

Full length article

Interface strain gradient enabled high strength and hardening in laminated nanotwinned Cu

Zhao Cheng^{a,1}, Tao Wan^{a,b,1}, Lei Lu^{a,*,2}

^a Shenyang National Laboratory for Materials Science, Institute of Metal Research, Chinese Academy of Sciences, Shenyang 110016, China

^b School of Materials Science and Engineering, University of Science and Technology of China, Shenyang 110016, China



ARTICLE INFO

Keywords:

Laminated nanotwin Cu
Extra strengthening
Interface strain gradient
Geometrically necessary dislocation
Interface spacing

ABSTRACT

Interfaces play a crucial role in mechanical behaviors of laminated materials. In this study, a series of hard/soft nanotwinned Cu laminates with varying interface spacing from 200 to 33 μm are prepared by means of direct current electrodeposition. Simultaneous improvement of strength and work hardening with decreasing interface spacing is found in tensile tests. Extra strengthening and geometrically necessary dislocations (GNDs), but without any strain concentration, are found in the vicinity of interfaces. An obvious strain discrepancy appears across the interface and decreases with decreasing interface spacing. Most importantly, a highest plastic strain gradient appearing in the vicinity of interfaces, regardless of interface spacing, indicates a significant deformation compatibility across the interfaces. The spatially-distributed strengthening mediated by interface contributes for increasing strength and decreasing strain discrepancy by decreasing the interface spacing.

1. Introduction

As typical heterogeneous nanostructured (HNS) materials, laminated metals with interfaces separating adjacent components have increasingly attracted attentions due to the higher strength, work hardening, ductility, toughness and their combination [1–6]. For example, Cu/CuZn laminates with coarse grained Cu layer and nanograined CuZn layer show simultaneous improvement of strength and ductility with decreasing interface spacing from 125 to 15 μm in tensile tests [7,8]. Layered metal composite (LMC) fabricated by hot-rolling and annealing of pure Ti and Al sheets exhibit high tensile ductility, being superior to any individual Ti or Al sheets [9,10]. Heterogeneous laminated Ti, prepared by asymmetric rolling and subsequent partial recrystallization, can have both the strength of the ultrafine grained component and the ductility of coarse grained component [11].

In order to interpret the attainment of both high strength and ductility in layered composites, several deformation mechanisms have been suggested, such as interface constraint [9,12], enhanced strain hardening [11], back stress strengthening [8,13], etc. Interfaces and the interface-mediated deformation are considered to play a crucial role in

the transferring loads and redistribution of stress during the deformation of layered components [9,14,15]. Originating from the mutual constraint between neighboring hard and soft layers in the laminated Cu/CuZn, dislocations nucleate in vicinity of interfaces inside coarse grained (soft) layers and some of them move to interfaces [16]. As a result, strong dislocation pile-up and serious strain concentration happen at interfaces, forming the interface affected zones (IAZs), which contributes for the improved strength of the laminated Cu/CuZn [8].

As for the LMC Ti/Al with different elastic modulus and deformation mechanisms between neighboring layers, the stress state of each layer is changed and stress partitioning happens, which activates the plastic deformation of brittle Ti layers [9]. In addition, Al layer can relieve the strain localization and restrict the development of microcrack due to the strong inter-constraint between neighboring layers. As a result, the LMC Ti/Al can exhibit superior ductility.

Researchers also found that the inhomogeneous deformation between soft and hard components can contribute to the strengthening and strain hardening of laminated structures according to the theory of strain gradient plasticity [17–19]. During deformation of laminated structures, soft components yield plastic deformation firstly due to the

* Corresponding author.

E-mail address: llu@imr.ac.cn (L. Lu).

¹ These authors contributed equally to this work.

² Lei Lu was an Editor of the journal during the review period of the article. To avoid a conflict of interest, Lei Lu was blinded to the record and another editor processed this manuscript.

lower yield strength while hard components yield later [20,21]. Thus, plastic strain discrepancy or strain gradient appears between soft and hard components. Geometrically necessary dislocations (GNDs) are necessarily produced as required to accommodate the strain gradient and contribute to strengthening and work hardening by producing kinematic hardening (back stress) or/and isotropic hardening (effective stress) [22–24]. Similarly, inhomogeneous plastic deformation related to the strain gradient and GNDs for superior mechanical properties has been generally validated in other HNS materials with gradient [25,26], bimodal [27,28] or harmonic [29,30] structures.

Homogeneous nanotwinned (HNT) structure has been regarded as desired prototypical structure for designing heterogeneous microstructure, such as gradient [26] and laminated [31] for clarifying their fundamental deformation mechanisms. One of the advantages of HNT components is the controllable microstructure, like grain size, twin thickness, and twin orientations. For example, HNT Cu with columnar grain and highly oriented nanoscale twins parallel to the growth surface have shown a strong anisotropic plastic deformation, where the dominant deformation mechanism can be effectively switched among three dislocation modes, namely dislocation glide in between the twins, dislocation transfer across twin boundaries, and dislocation-mediated boundary migration, by changing the loading orientation with respect to the twin planes [32,33].

By using 4 HNT structures with increasing grain size and twin thickness as the different individual components (Ⓐ, Ⓑ, Ⓒ & Ⓓ), we built a series of gradient nanotwinned (GNT) Cu for unraveling the structural gradient induced strengthening, hardening and the unique deformation mechanism [26,34,35]. It has been revealed that GNT Cu not only exhibits obvious extra strengthening and work hardening, comparing to their freestanding HNT components, but also indicates novel bundles of concentrated dislocations (BCDs) mediated deformation mechanisms. These BCDs are formed by accumulation of GNDs which accommodates for the strain gradient across 4 components. Meanwhile BCDs or GNDs produce strong back stress rather than effective stress, as the origin of the extra strengthening of GNT Cu [34].

Further, we use only two HNT components, namely hard Ⓐ and soft Ⓑ, to design three types of representative HNS materials with different volume fractions of GTLs (f_g) of 10% (laminated), 50% (half gradient) and 100% (full gradient) while both rule-of-mixture strength and overall structural gradient are constant for quantitatively revealing f_g effect on the extra strengthening behaviors [36]. With increasing f_g up to 100%, the yield strength of GNT Cu samples can be improved without loss of uniform elongation. The strengthening mechanism originates from the more broadly-distributed strain gradient and resultant widely distributed GNDs. However, the fundamental strengthening mechanism, including the interface spacing related both plastic strain gradient and strain discrepancy, of laminated nanotwinned (LNT) Cu is still unknown.

In this study, we focus on the study of LNT structures with only two components, hard Ⓐ and soft Ⓑ, but with varying interface spacings, to unravel the intrinsic incompatible plastic deformation and resultant strengthening of interfaces under tensile tests. To figure out the plastic deformation, strain discrepancy between hard and soft component and strain gradient distribution across the interfaces and their evolutions with increasing tensile strains of LNT Cu were quantitatively studied by means of the full-filed strain technology. Correspondingly, deformation microstructure, especially the distribution and configuration of GNDs of LNT Cu were characterized by combining electron backscatter diffraction (EBSD) with dual-beam diffraction technique. The stress partitioning analysis on back stress and effective stress was conducted for LNT Cu and HNT components to clarify the origin of the extra strengthening. Finally, the interface-mediated deformation strengthening mechanisms of LNT Cu were discussed.

2. Experimental

2.1. Design and preparation of LNT Cu samples

Two HNT structures, hard Ⓐ and soft Ⓑ, with typical columnar grains embedded preferentially orientated nanotwins were used to build LNT Cu samples. As the same microstructures reported in [26], hard Ⓐ has small grain size (2.5 μm) and twin thickness (29 nm) while soft Ⓑ has larger ones (15.8 μm and 72 nm). As illustrated in Fig. 1a1, we prepared a series of LNT Cu consisting of periodically stacked ⒶⒷⒶ components, and the interface spacing l decreases proportionally from 200 to 33 μm . LNT Cu with $l = 200 \mu\text{m}$ is named as LNT-200, other samples are defined in the same way, as shown by Figs. 1b1, c1 and d1. Noted that Ⓐ is at the surface as always [37], and hard Ⓐ and soft Ⓑ have the same volume fraction (50%) for all LNT Cu samples, which have a constant total sample thicknesses of $\sim 400 \mu\text{m}$.

The direct-current electrodeposition technique was used to prepare LNT Cu samples and their freestanding HNT components. The current density and total deposition time were kept at 30 mA/cm² and 16 h, respectively. More details about the setup and the parameters can be found in [26]. HNT-Ⓐ and HNT-Ⓑ samples were electrodeposited at constant electrolyte temperature at 20 and 35 °C, respectively. LNT Cu samples were prepared in two electrolytic tanks with electrolyte temperature at 20 and 35 °C, respectively. For example, LNT-200 was deposited firstly in 20 °C tank for 4 h, then in 35 °C tank for 8 h, and finally in 20 °C tank for 4 h. That means a total deposition period (25–35–25 °C) is 16 h. Compared to LNT-200, LNT-100, LNT-50, and LNT-33 underwent two, four and six temperature periods in the same total deposition time (16 h), respectively.

2.2. Microstructures characterization

The cross-sectional microstructures of as-deposited LNT Cu were characterized via a FEI Nova NanoSEM 450 field emission gun scanning electron microscope (SEM) with backscattering electron imaging (BSE) mode. A fixed region on cross-section of LNT-50, which was deformed at the applied strain ranging from 0, 1% to 5%, was successively measured by electron backscatter diffraction (EBSD) with a step size of 100 nm in the SEM under a voltage of 20 kV. The Kernel average misorientation (KAM) was mapped by Oxford HKL channel 5 software. The local dislocation density is calculated by $\rho = 2\theta/lb$ where l is the unit length (100 nm) and b is the Burgers vector (0.255 nm for Cu) [7]. The local misorientation θ of a given point was calculated by using 3×3 filter size. Here the calculation just takes care of θ lower than 3°, which is defined as a threshold misorientation for grain boundary. Before SEM and EBSD observation, the specimen was mechanically polished and then electrochemically polished in an electropolishing solution of phosphoric acid (25%), alcohol (25%), and deionized water (50%) at ambient temperature.

The cross-sectional microstructure of deformed LNT Cu samples was examined by a transmission electron microscope (TEM, FEI Tecnai G2 F20) operated at 200 kV. Mode I and Mode II dislocations were identified by a dual beam diffraction TEM technique under diffraction vectors of $\mathbf{g}_T = 111$ and $\mathbf{g}_T = 200$, respectively. Before TEM observations, the specimen was thinned by twin-jet electrochemical polishing in the electropolishing solution at about $-10 \text{ }^\circ\text{C}$.

2.3. Microhardness measurement

The cross-sectional hardness distribution along depth of as-deposited LNT Cu samples were measured on a Qness Q60 A+ microhardness tester with a Vickers indenter at a load of 50 g and dwell time of 10 s. A small load of 10 g was used to measure the hardness near interfaces of LNT-200 before and after tensile deformation. Such small load can promote denser indentation measurement for accurately detecting hardness distribution near interfaces, but might result in a slightly

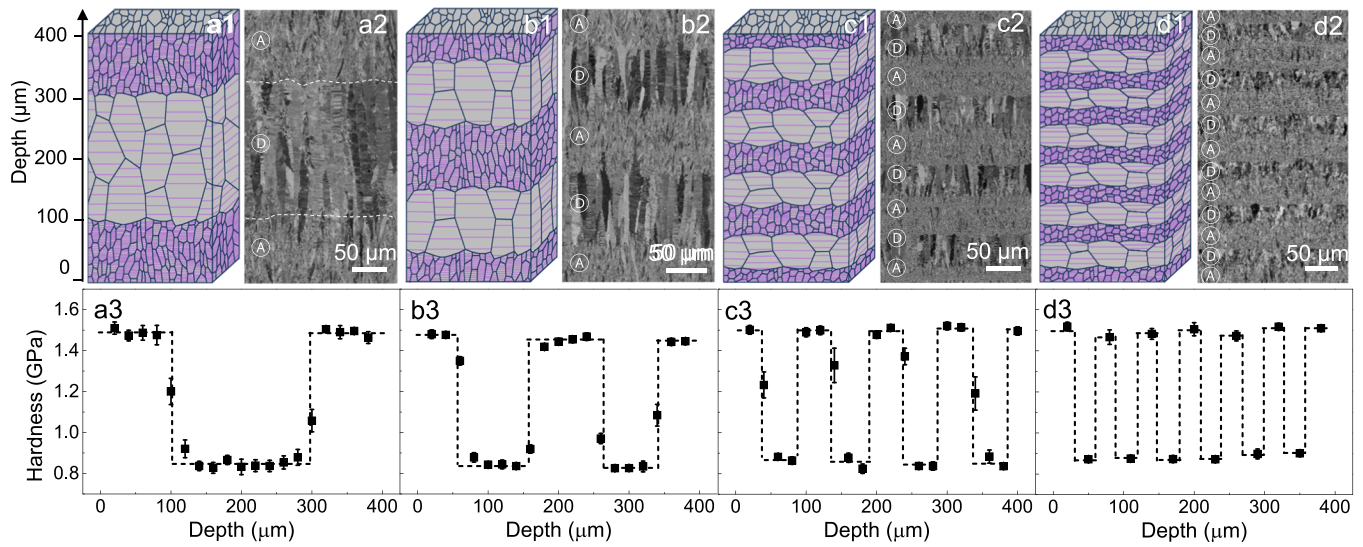


Fig. 1. The schematic, cross-sectional SEM image and hardness distribution of LNT-200 (a1-a3), LNT-100 (b1-b3), LNT-50 (c1-c3) and LNT-33 (d1-d3) composed of hard \textcircled{A} and soft \textcircled{B} components with interface spacing of 200, 100, 50 and 33 μm , respectively. (For interpretation of the references to color in this figure legend, the reader is referred to the web version of this article.)

higher hardness due to the indentation size effect [38]. Before hardness measurement, these specimens were mechanically polished first and then electrochemically polished. At least five indents were measured to get the average hardness at a given depth.

2.4. Uniaxial and loading-unloading-reloading tensile tests

The gage area of the dog bone-shaped flat tensile specimens was 5 mm \times 2 mm, the specimens were cut from the as-deposited HNT Cu and LNT Cu sheets by using electric spark machine, then followed by mechanically and electrochemically polished. Uniaxial tensile tests were carried on an Instron 5848 microtester with a contactless MTS LX300 laser extensometer at a strain rate of $5 \times 10^{-3} \text{ s}^{-1}$ at room temperature. Tensile tests for each sample were repeated at least three times to ensure the data reproducibility.

The loading-unloading-reloading tensile tests of HNT Cu and LNT Cu samples were performed on Instron 5848 microtester and a contactless strain gaging system based on digital image correlation (DIC) was used to measure the strain. The loading (or reloading) and unloading were controlled by the crossover displacement at a strain rate of $1 \times 10^{-3} \text{ s}^{-1}$ and by the load force at a stress rate of 70 N/min with the unloading limit of 10 N, respectively. Back stress σ_b and effective stress σ_{eff} can be calculated according to the classical Dickson's method [39,40]

$$\sigma_b = \frac{\sigma_f + \sigma_{ry}}{2} - \frac{\sigma^*}{2} \quad (1)$$

$$\sigma_{eff} = \sigma_f - \sigma_b \quad (2)$$

where σ_f is the true flow stress before unloading, σ^* is the stress interval past the peak stress after unloading, and σ_{ry} is the reverse yield stress upon unloading. σ_{ry} is determined by the line with a slope of elastic modulus E ($\sim 120 \text{ GPa}$ for Cu) and an offset strain δ (0.01%) intercepting the unloading curve.

2.5. Characterization of strain distribution

An Olympus LEXT OLS4100 confocal laser scanning microscope (CLSM) with a planar resolution of 120 nm and a height resolution of 10 nm was used to ex-situ measure the height of the lateral surface (x - y plane as indicated in Fig. 1a) of each tensile specimen after unloading. During the CLSM measurement, a homemade fixture was used to avoid

the tensile specimen tilting.

From the measured distribution of lateral surface heights of each tensile specimen, the average profile of lateral surface height at a given depth or y was obtained by calculating the mean value of lateral surface heights along the x direction. Then the net change of height profile $\Delta H(y)$ was obtained by subtracting the average profiles before tensile deformation from that after tensile deformation. Hence, the relative lateral plastic strain $\Delta \varepsilon_z^p$ at a given y is calculated by

$$\Delta \varepsilon_z^p(y) = \frac{2\Delta H(y)}{W} \quad (3)$$

where W is the width of tensile sample before deformation. The position with the smallest absolute value $|\Delta H|$ is offset to zero as the reference point. The largest difference in lateral strain between soft and hard in every period, $\Delta \varepsilon_z^{p,A-D}$, is obtained from the height difference according to Eq. (3). The lateral strain gradient η_z is estimated by differentiating the smoothed profile of $\Delta \varepsilon_z^p(y)$.

3. Results and discussion

3.1. Microstructures and tensile properties of LNT Cu

As expected, four well controlled LNT Cu samples are prepared and their cross-sectional microstructures are shown in SEM images in Fig. 1. LNT-200 exhibits a typical sandwich structure with soft \textcircled{B} in the core and hard \textcircled{A} at both surfaces (Fig. 1b2). The interfaces between two components are well bonded and the interface spacing l is 200 μm . Along the depth of LNT-200, the hardness jumps at interfaces from 1.5 GPa (\textcircled{A}) into 0.85 GPa (\textcircled{B}) and its distribution likes a rectangular wave as shown in Fig. 1a3. Compared to LNT-200, LNT-100 has 2 periods of $\textcircled{A}\textcircled{B}\textcircled{A}$ stacking with 4 interfaces and the interface spacing decreases into 100 μm (Fig. 1b2). The hardness distribution also exhibits two rectangular waves (Fig. 1b3). Similarly, LNT-50 (Figs. 1c2 and c3) and LNT-33 (Figs. 1d2 and d3) shows 4 and 6 periods of microstructure and hardness distribution, and the interface spacing decreases into 50 μm and 33 μm , respectively.

Fig. 2a shows the tensile engineering stress-strain curves of four LNT Cu samples in comparison to their HNT components \textcircled{A} and \textcircled{B} . HNT- \textcircled{A} has a yield strength ($\sigma_Y=446 \text{ MPa}$) and a limited uniform elongation (1.6%) while HNT- \textcircled{B} has a lower yield strength ($\sigma_Y=221 \text{ MPa}$) with larger uniform elongation (21.7%). The yield strength of LNT-200 is 366

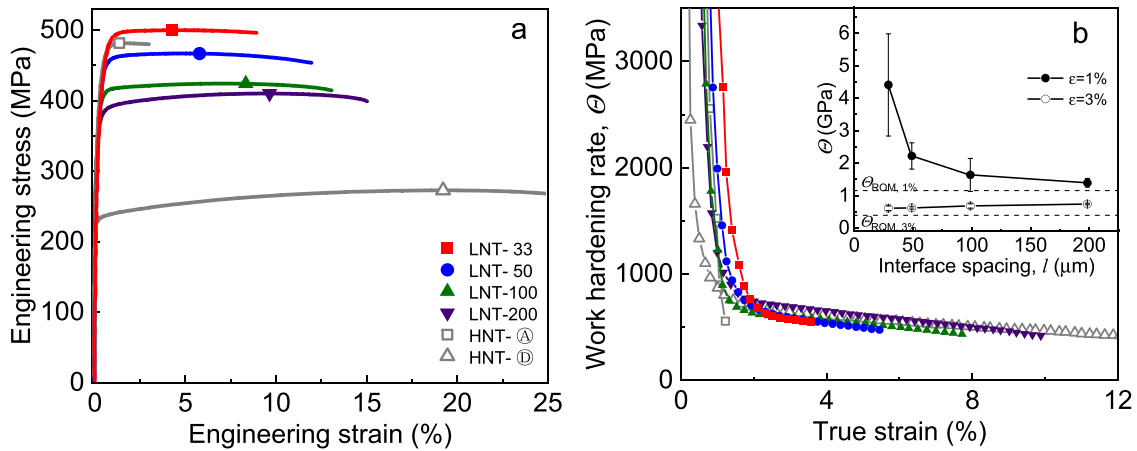


Fig. 2. Engineering stress-strain curves (a) and work hardening rate Θ -true strain curves (b) of LNT Cu compared with HNT-⊕ and HNT-⊙. The inset in (b) shows the work hardening rates at true strains $\epsilon = 1\%$ and 3% of LNT Cu with various interface spacing l . The dash lines represent the rule-of-mixture (ROM) work hardening rates at $\epsilon = 1\%$ and 3% as indicated. (For interpretation of the references to color in this figure legend, the reader is referred to the web version of this article.)

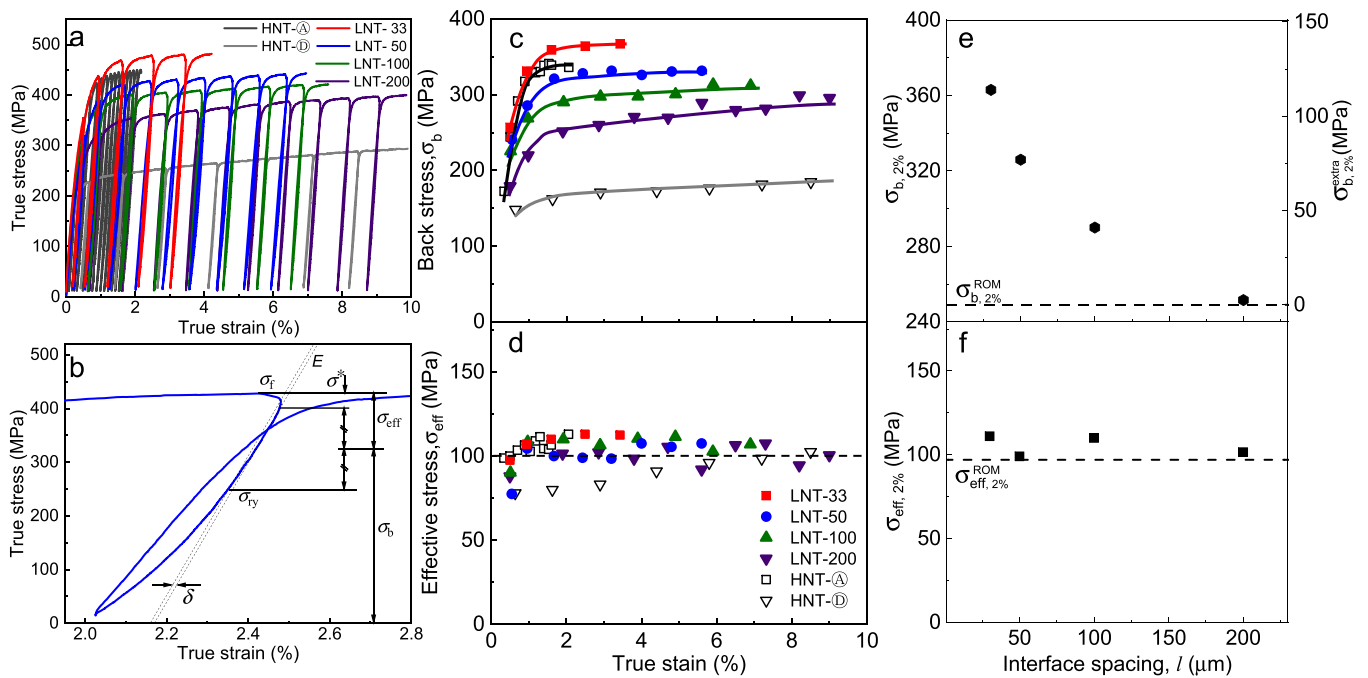


Fig. 3. (a) True stress-strain curves of loading-unloading-reloading (LUR) tests for LNT Cu in comparison to HNT Cu. (b) Definition of back stress, σ_b and effective stress, σ_{eff} at unloading based on Dickson's method in a magnified unloading-reloading loop of LNT-50 sample. The variation of back stress (c) and effective stress (d) with true strains of HNT Cu and LNT Cu. (e) Back stress, $\sigma_{b,2\%}$ (y axis on the left) and the extra back stress $\sigma_{b,2\%}^{extra}$ (y axis on the right) at true strain of 2% as a function of layer thickness. (f) Effective stress at true strain of 2%, $\sigma_{eff,2\%}$, varies with interface spacing l . The dash lines in (e) and (f) represent ROM back stress $\sigma_{b,2\%}^{ROM}$ and ROM effective stress $\sigma_{eff,2\%}^{ROM}$ by averaging two HNT Cu, respectively. (For interpretation of the references to color in this figure legend, the reader is referred to the web version of this article.)

MPa, which is slightly higher than the rule-of-mixture (ROM) yield strength ($\sigma_Y^{ROM}=334$ MPa) by averaging the yield strengths of HNT-⊕ and HNT-⊙, resulting in an extra yield strength $\sigma_Y^{extra}=32$ MPa. From LNT-200 to LNT-33, the yield strength increases substantially up to 450 MPa but the uniform elongation decreases. Noted that the yield strength of LNT-33 with the smallest interface spacing surpasses that of HNT-⊕, showing the highest σ_Y^{extra} (116 MPa). Meanwhile, the uniform elongation of LNT-33 is also larger than that of HNT-⊕, indicating a better combination of strength and ductility.

Fig. 2b displays the work hardening curves of HNT Cu and LNT Cu. The two typical stages of work hardening can be clearly seen: the work

hardening rate decreases quickly at small strains in the elastic to plastic stage (here called stage II) after elastic deformation stage and the decrease becomes gentle at larger strains in the steady plastic deformation stage (stage III), as defined by [41]. HNT-⊕ has high work hardening rate in stage II but without stage III while HNT-⊙ has a lower stage II and longer stage III. The work hardening rate at stage II in LNT-200 is close to that of hard ⊕ and becomes larger from LNT-200 to LNT-33. As shown in the inset of Fig. 2b, the work hardening rate at applied strain $\epsilon = 1\%$ in LNT Cu is higher than ROM value by averaging HNT-⊕ and HNT-⊙ (indicated by the dash line), showing an extra work hardening induced by LNT structure. Moreover, such extra work

hardening increases substantially with decreasing interface spacing, consistent with the improvement of yield strength. However, the work hardening at stage III becomes slightly lower and shorter from LNT-200 to LNT-33. The work hardening rate at a large strain $\varepsilon = 3\%$ in LNT Cu is slightly higher than the ROM value and keeps almost constant as the interface spacing decreases (the inset of Fig. 2b). This indicates the extra work hardening of LNT Cu mainly happens in the initial deformation stage.

3.2. Back stress and effective stress of LNT Cu

To further unravel the origin of the extra strengthening, we measured back stress and effective stress by partitioning the flow stress of LNT Cu in comparison to HNT Cu. The loading-unloading-reloading tensile tests were performed to measure back stress and effective stress of LNT Cu by using classic Dickson's method [39,40]. From Fig. 3a, the flow stress increases substantially from LNT-200 to LNT-33 and the flow stress of LNT-33 even surpasses that of HNT-Ⓐ, all of which are consistent with the results of continuous tension tests in Fig. 2a.

We take a branch of loading-unloading-reloading tensile curve of LNT-50 as an example to show the stress-strain response of LNT Cu samples, as shown in Fig. 3b. Upon unloading after deformation at $\varepsilon = 2.4\%$, LNT-50 sustains a transient elastic deformation and quickly yields. The unloading curves noticeably deviates from the elastic unloading despite the applied stress remains tensile. Such a premature yielding at unloading is also called Bauschinger's effect [42], as an indicator of the presence of strong back stress. After partitioning flow stress based on the unloading curve, we clearly see that the back stress is much larger than the effective stress.

As references for LNT Cu, the back stress and effective stress of two HNT Cu samples are introduced firstly. As shown in Fig. 3c, the back stress of HNT-Ⓐ increases quickly at initial deformation and reaches a saturated value of 336 MPa at $\varepsilon = 2\%$ ($\sigma_{b,2\%}$), which accounts 75% for the flow stress of HNT-Ⓐ. The back stress of HNT-Ⓞ has similar increment with straining but $\sigma_{b,2\%}$ slows down to 163 MPa, which still contributes 65% for the flow stress of HNT-Ⓞ. Such high back stress of HNT Cu sample has been reported and is attributed to incompatible deformation between twin and matrix [34].

Back stresses of all LNT Cu samples also increase quickly at small strains and moderately after $\varepsilon = 2\%$. $\sigma_{b,2\%}$ of LNT-200 is 252 MPa, contributing 72% for the flow stress. From LNT-200 to LNT-33, $\sigma_{b,2\%}$ increases substantially. Noted that as for LNT-33 with the smallest interface spacing, $\sigma_{b,2\%}$ reaches 363 MPa, almost 78% of flow stress. Both the absolute value and the relative value of back stress surpass that of HNT-Ⓞ.

In contrary to back stress, the effective stress of LNT Cu is less sensitive to the interface spacing, seeing Fig. 3d. The effective stress of HNT Cu increases quickly into a saturated value (~ 100 MPa) at $\varepsilon = 2\%$. From LNT-200 to LNT-33, the saturated effective stress also varies slightly and keeps around 100 MPa.

Fig. 3e further shows the variation of $\sigma_{b,2\%}$ (left axis) and the extra back stress $\sigma_{b,2\%}^{\text{extra}} = \sigma_{b,2\%} - \sigma_{b,2\%}^{\text{ROM}}$ (right axis) of LNT Cu samples at $\varepsilon = 2\%$ as a function of the interface spacing. The extra back stress $\sigma_{b,2\%}^{\text{extra}}$ is estimated by averaging $\sigma_{b,2\%}$ of HNT-Ⓐ and HNT-Ⓞ, as marked by the horizontal dash line. Obviously, $\sigma_{b,2\%}$ of all LNT Cu samples are higher than $\sigma_{b,2\%}^{\text{ROM}}$ and increase substantially as the interface spacing decreases. $\sigma_{b,2\%}^{\text{extra}}$ is as high as 114 MPa in LNT-33 and is comparable to its $\sigma_{Y}^{\text{extra}}$ (Fig. 2a). In addition, the effective stresses $\sigma_{\text{eff},2\%}$ of LNT Cu samples are independent on the interface spacing and comparable to its $\sigma_{\text{eff},2\%}^{\text{ROM}}$, as shown in Fig. 3f. These results indicate the extra strengthening of LNT Cu stems substantially from the improvement of back stress instead of effective stress.

3.3. Gradient strains across interfaces in LNT Cu

The characterization of gradient strain across the interfaces between neighboring components can offer the insight into the intrinsic deformation mechanism [35]. As illustrated in Fig. 4a, the height on lateral surface (x-z plane) was measured to calculate the distribution of ε_y of LNT Cu. The lateral surface of as-prepared LNT-200 sample are quite flat except for a negligible variation arising from the mechanical polishing, as shown in Fig. 4b1. After deformation at $\varepsilon = 3\%$ (Fig. 4b2), the height of component Ⓞ is lower than that of component Ⓐ. By averaging height along the tensile direction (x axis), the average height profile across the sample thickness (z axis) is shown in Fig. 4b3. The average height keeps constant across all sections of as-prepared LNT-200, but becomes lower in the core at $\varepsilon = 3\%$. The net change of height profile can be obtained by subtracting the original height profile before deformation from that after deformation. By using Eq. (3), we attain the distribution of relative lateral strain $\Delta\varepsilon_y^p$, as shown in Fig. 4b4. The absolute $|\Delta\varepsilon_y^p|$ increases gradually across the interface from Ⓐ to Ⓞ. $|\Delta\varepsilon_y^p|$ reaches maximum in the middle of component Ⓞ and minimum at surface of component Ⓐ, both of which are at positions of roughly half of interface spacing ($l/2$) away from the interface. The largest lateral strain discrepancy between Ⓐ and Ⓞ, $\Delta\varepsilon_y^{p,A-D}$, reaches 0.16% for LNT-200 (Fig. 4b4).

By smoothing and differentiating the curve of $\Delta\varepsilon_y^p$ in Fig. 4b4, we obtain the distribution of strain gradient η_y in Fig. 4b5, where η_y reaches the largest (21 m^{-1}) at interfaces, decreases gradually away from the interface, and becomes ~ 0 in the middle of component Ⓞ or at surfaces of component Ⓐ. The width of the area covered by the non-zero strain gradient on both sides of the interface is defined as the IAZ with a thickness larger than $100 \mu\text{m}$ for LNT-200, which is indicated by red region in Fig. 4b5.

Similarly, LNT-100 also exhibits typical gradient deformation, as shown in Figs. 4c1-c5. Compared to the relative flat lateral surface (Fig. 4c1) of as-prepared LNT-100, the height contour of LNT-100 at $\varepsilon = 3\%$ exhibits two-period variations (Fig. 4c2), consistent with their component stacking (Fig. 1b1). By comparing the average height profiles before and after deformation (Figs. 4c3 & 4c4), two typical triangle peaks of $\Delta\varepsilon_y^p$ are also observed at the position of $\sim l/2$ away from interface between component Ⓞ and Ⓐ, respectively. $\Delta\varepsilon_y^{p,A-D}$ of LNT-100 is 0.09%, which is smaller than that of LNT-200. From Fig. 4c5, the whole section is almost covered by non-zero η_y , i.e., IAZs spreads all over the LNT-100 sample along thickness. The largest η_y still appears at the interfaces and gradually decreases away from the interfaces.

The distributions of height and $\Delta\varepsilon_y^p$ of LNT-50 and LNT-33 are shown in Figs. 4d1-d5 and 4e1-e5, respectively. At $\varepsilon = 3\%$, both deformed samples exhibit multiple-periodic gradient-distributed height and $\Delta\varepsilon_y^p$. $\Delta\varepsilon_y^{p,A-D}$ decreases from 0.04% to 0.03% when the interface spacing decreases from 50 to 33 μm .

Fig. 4f and 4g summary the variation of $\Delta\varepsilon_y^{p,A-D}$ and η_y at interfaces of LNT Cu with varying interface spacing, respectively. As shown in Fig. 4f, $\Delta\varepsilon_y^{p,A-D}$ decreases with decreasing interface spacing. That means the incompatible deformation between different components is reduced with decreasing the interface spacing. Interestingly, η_y at interfaces of 4 LNT Cu samples almost keeps constant $\sim 20 \text{ m}^{-1}$, which suggests that η_y is a salient feature of interfaces, independent on the interface spacing.

3.4. Interface-mediated hardening of LNT Cu

We take LNT-200 as an example to further characterize the deformation behavior by measuring the hardness distribution across the vicinity of interface before and after tension. The net hardness increment ΔH at a given position can be estimated by

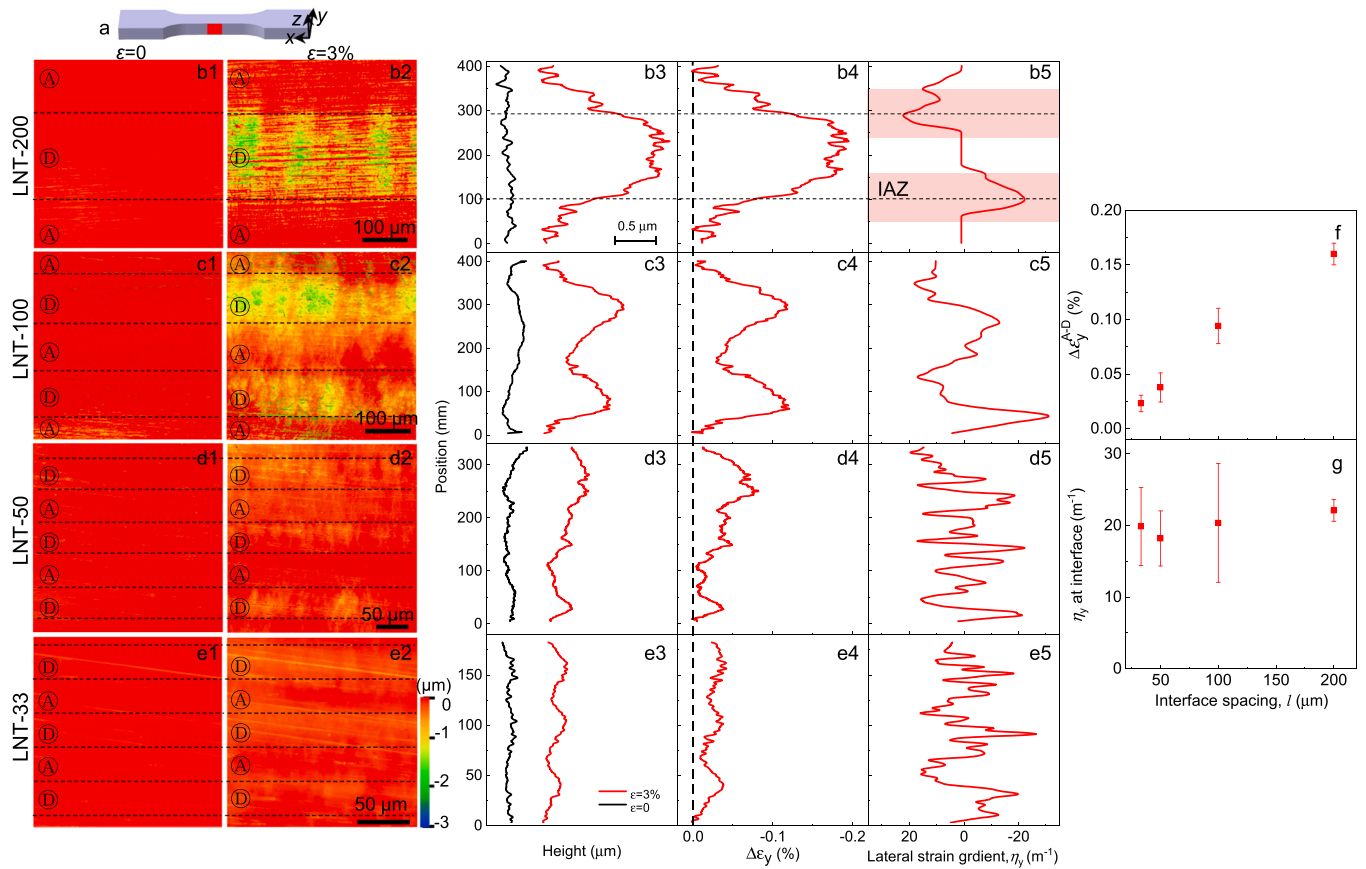


Fig. 4. Characterization of gradient lateral strain of LNT Cu. (a) Illustration of height profile on the lateral surface (x - z plane) measured by CLSM, where x , y and z axes are indicated. The measured height contour on the lateral surface of LNT-200 deformed at $\varepsilon = 0$ (b1) and $\varepsilon = 3\%$ (b2). (b3) Average height profiles at $\varepsilon = 0$ and 3% , as obtained from (b1) and (b2), respectively. The distribution of relative lateral strain $\Delta\varepsilon_y^p$ (b4) and lateral strain gradient (b5) of LNT-200. (c1-c5), (d1-d5) and (e1-e5) are same as (b1-b5) except for LNT-100, LNT-50 and LNT-33, respectively. The variation of lateral strain difference between component \textcircled{A} and \textcircled{D} $\Delta\varepsilon_y^{p,A-D}$ (f) and lateral strain gradient η_y at interface (g) with interface spacing l . (For interpretation of the references to color in this figure legend, the reader is referred to the web version of this article.)

$$\Delta H = H - H_0 \quad (4)$$

where H and H_0 are the hardness after and before tensile deformation, respectively. Comparing the results in Figs. 5a1 and 5a2, the hardness of HNT- \textcircled{A} almost keeps the same at both $\varepsilon = 0$ and $\varepsilon = 1\%$, which means ΔH of HNT- \textcircled{A} is near zero, as indicated by horizontal dash line in Fig. 5a2, which is consistent with its limited work hardening capacity (Fig. 2b). Component \textcircled{A} in LNT-200 also exhibits a negligible hardness increment at applied strains from $\varepsilon = 1\%$ to $\varepsilon = 5\%$, as shown in Figs. 5b1 and 5b2.

However, the hardness of component \textcircled{D} in both HNT- \textcircled{D} and LNT-200 increase substantially with increasing strain, as shown in Figs. 5b1 and 5c1. As seen in Fig. 5c2, the average ΔH of HNT- \textcircled{D} at $\varepsilon = 1\%$ is 0.03 GPa, which is obviously lower than ΔH (0.09 GPa at interface) of \textcircled{D} in LNT-200. As a result, an extra ΔH (0.06 GPa at interface) of component \textcircled{D} is produced in LNT-200 at $\varepsilon = 1\%$, as indicated by shadow between solid and dash lines in Fig. 5b2. Interestingly, the peak values of ΔH (and the extra hardening) reaches at the interface and decreases gradually away from the interface. As the applied strain increases up to $\varepsilon = 5\%$, ΔH and corresponding extra hardening at the interface increase noticeably to 0.2 GPa and 0.09 GPa, respectively.

3.5. Dislocation behaviors at interfaces in LNT Cu

The interface-mediated strengthening or hardening is closely related to the GNDs storage as a geometrical requirement for accommodating strain gradient according to the theory of strain gradient plasticity

[17–19]. EBSD and TEM observations of LNT-50 are further performed to detect the interface mediated dislocation behaviors. From the EBSD orientation mapping for the region across interfaces of as-prepared LNT-50 (Fig. 6a1), most of grains in component \textcircled{A} and \textcircled{D} exhibit strong (111) texture due to presence of the preferentially orientated TBs. Nearby the interface, component \textcircled{D} has large columnar grains, but component \textcircled{A} has tiny grains with random orientation, implying a huge discrepancy in microstructure beside the interface.

Comparing the EBSD mappings of LNT-50 at $\varepsilon = 1\%$ (Fig. 6b1) and $\varepsilon = 5\%$ (Fig. 6c1) to the as-deposited one (Fig. 6a1), no significant changes in grain morphologies are observed. But dislocation densities are improved substantially in components \textcircled{A} and \textcircled{D} , especially at interfaces, seeing Figs. 6b2 and 6c2 relative to Fig. 6a2. By averaging the dislocation density at a given position, we obtain the distribution of average dislocation density across the interface in LNT-50, as shown in Fig. 6d. Before deformation, the dislocation density of component \textcircled{A} is slight higher than that of component \textcircled{D} . At $\varepsilon = 1\%$, there is a peak of dislocation density at the interface, i.e., dislocation density at the interface is higher than that in component \textcircled{A} or \textcircled{D} . Peak value increases with increasing strain. As the applied strain increases up to $\varepsilon = 5\%$, the peak of dislocation density is as high as 10^{15} m^{-2} at the interface.

The dislocation morphologies near the interfaces of LNT-50 at $\varepsilon = 3\%$ are examined by TEM, as shown in Fig. 7. Low-magnification TEM image in Fig. 7a shows a sharp interface (dash lines) between component \textcircled{A} and \textcircled{D} . As the grain size of component \textcircled{D} is more than $20 \mu\text{m}$ along the direction perpendicular to the interface (or TBs), so the dislocation morphologies near the interface (labeled 1 in Fig. 7a) and $\sim 15 \mu\text{m}$ far

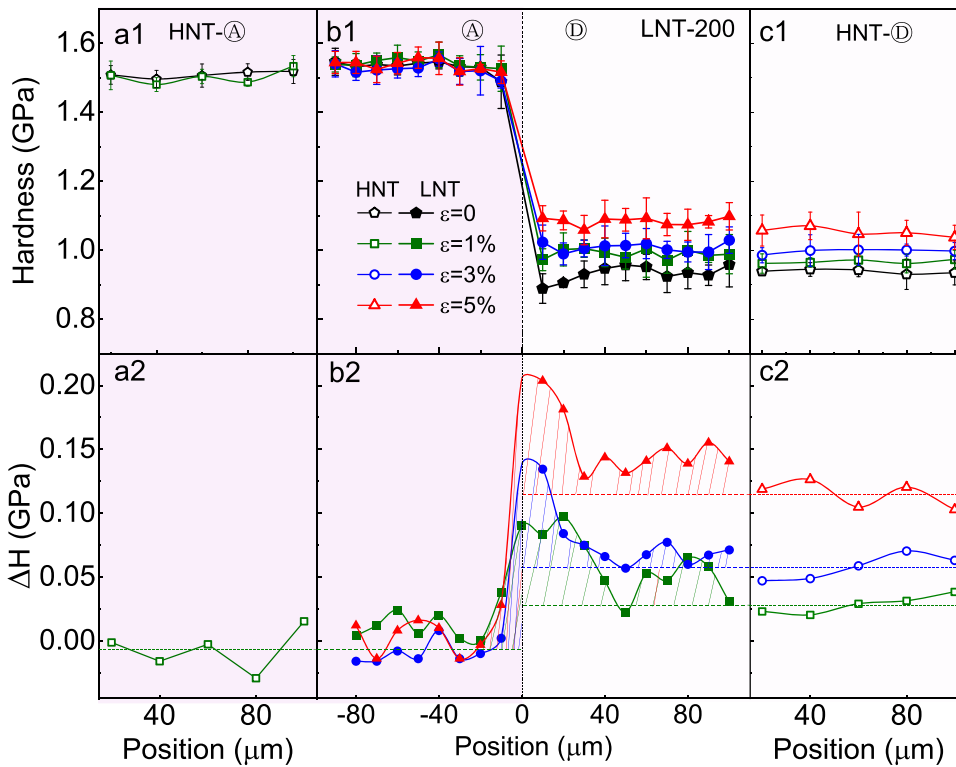


Fig. 5. The hardening of soft \textcircled{C} and hard \textcircled{A} components in LNT Cu in comparison to corresponding HNT Cu samples. Hardness distribution of HNT- \textcircled{C} (a1), LNT-200 (b1) and HNT- \textcircled{C} (c1) at tensile strains $\varepsilon = 0, 1\%, 3\%$ and 5% . (a2-c2) are same as (a1-c1) except for the hardening ΔH defined as the hardness increment after deformation relative to that before deformation. The position at zero in (b1 and b2) indicates the position of interface. The horizontal dashed lines in (a2-c2) indicate the average hardening of HNT- \textcircled{A} and HNT- \textcircled{C} at different applied strains. The shadows in (b2) indicate the extra hardening of LNT-200 relative to HNT Cu. (For interpretation of the references to color in this figure legend, the reader is referred to the web version of this article.)

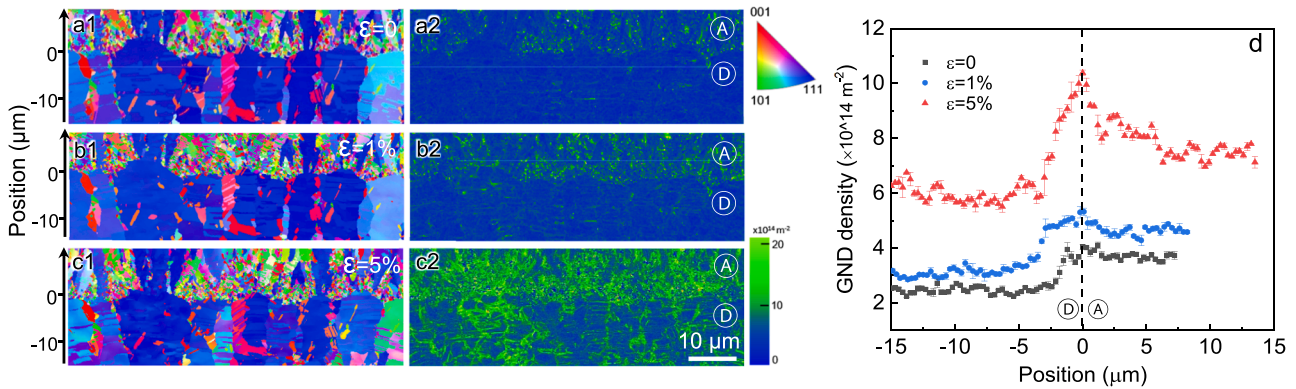


Fig. 6. EBSD orientation mapping (a1, b1, c1), corresponding dislocation density mapping (a2, b2, c2) and the average dislocation density variation (d) across the interface of LNT-50 at $\varepsilon = 0, 1\%, 5\%$. The dashed line in (d) indicates the position of interface. (For interpretation of the references to color in this figure legend, the reader is referred to the web version of this article.)

away from the interface (labeled 2) are characterized, respectively.

As shown in Figs. 7b-d, Region 1 has a lot of dislocation lines traversing multiple twin lamellae or piled up at TBs. Mode I dislocations with both glide plane and direction inclined to TBs [33] are identified by green arrows in Fig. 7c under diffraction vector of $\mathbf{g}_T = \mathbf{g}_M = 111$. The density of Mode I dislocation is about $4.1 \times 10^{13} \text{ m}^{-2}$. Mode II dislocations (orange arrows) with glide plane inclined to TBs but glide direction parallel to TBs are identified by the diffraction vector of $\mathbf{g}_T = 200$ (Fig. 7d). Recently, Mode II dislocations have been further revealed as tans-twin dislocations which can span multiple nanotwin lamellae on the corrugated slip planes [43]. Mode II dislocation density is estimated as $0.8 \times 10^{13} \text{ m}^{-2}$, which is lower than Mode I dislocation. Mode I dislocations are less observed in HNT Cu [32,33] but prominently in LNT Cu, which might be related to the nucleation sites [26] and feasible stress state [44] at interfaces for Mode I dislocations.

Dislocation morphology far away from the interface is quite different. First, sporadic dislocations traversing multiple twin lamellae

are observed in Fig. 7e. These dislocations are identified as Mode I dislocations from TEM image under diffraction vector of $\mathbf{g}_T = \mathbf{g}_M = 111$ in Fig. 7f and the dislocation density is estimated as $0.6 \times 10^{13} \text{ m}^{-2}$, which is one-magnitude lower than that in Region 1 (Fig. 7c). Whereas Mode II dislocation debris are clearly observed in Fig. 7g and the dislocation density is estimated as $3.0 \times 10^{13} \text{ m}^{-2}$, which is higher than that near the interface (Fig. 6d). From above TEM observations, the total dislocation density near the interface is higher than that away the interface.

3.6. Interface-mediated deformation mechanism of LNT Cu

Above experimental results clearly indicate that the extra strengthening of LNT Cu increases with decreasing the interface spacing, consistent with the results of laminated structures without nanotwins [4, 7-10,45,46]. For a better understanding on the strengthening mechanisms of laminated metals, we normalized the extra strength as

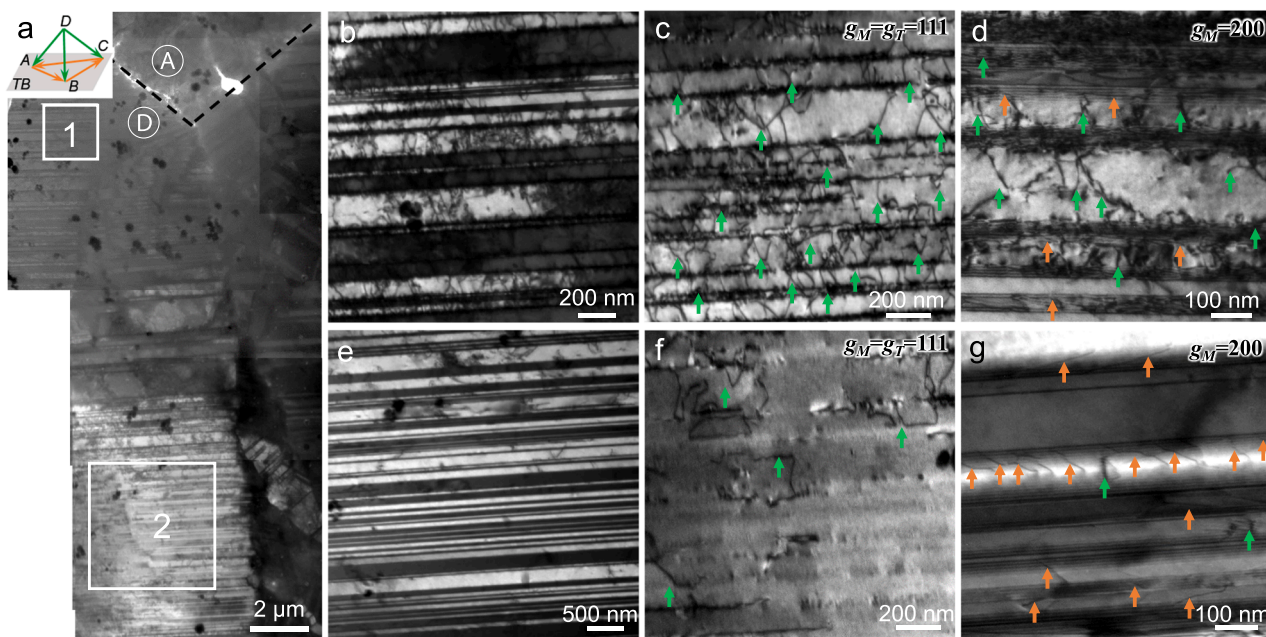


Fig. 7. Dislocation morphologies near and away from interface in LNT-50 at $\epsilon = 3\%$. (a) Low-magnification TEM image across the interface. The white rectangle region 1 and 2 in (a) are magnified into (b, c, d) and (e, f, g), respectively. (c, f) and (d, g) are imaged using two-beam diffraction with vectors of $\mathbf{g}_M = \mathbf{g}_T = 111$ and $\mathbf{g}_M = 200$, respectively. The black dash line in (a) outlines the interface between component A and B. Mode I and Mode II dislocations are indicated by green and orange arrows, respectively. (For interpretation of the references to color in this figure legend, the reader is referred to the web version of this article.)

$\sigma_Y^{extra}/\sigma_Y^{ROM}$ of different samples in the literature and summarized all data in Fig. 8. Taking the laminated Cu/Cu10Zn as an example, the extra strengthening of conventional laminated materials is getting obvious ($\sigma_Y^{extra}/\sigma_Y^{ROM}=4\%$) only when the interface spacing is less than $25 \mu\text{m}$ [7,

8]. As the interface spacing further decreases into $3.7 \mu\text{m}$, $\sigma_Y^{extra}/\sigma_Y^{ROM}$ increases up to 23% [8]. However, the curve of $\sigma_Y^{extra}/\sigma_Y^{ROM}$ vs. the interface spacing of LNT Cu lies above the data of conventional laminated materials, and the extra strengthening reaches about 35% at an

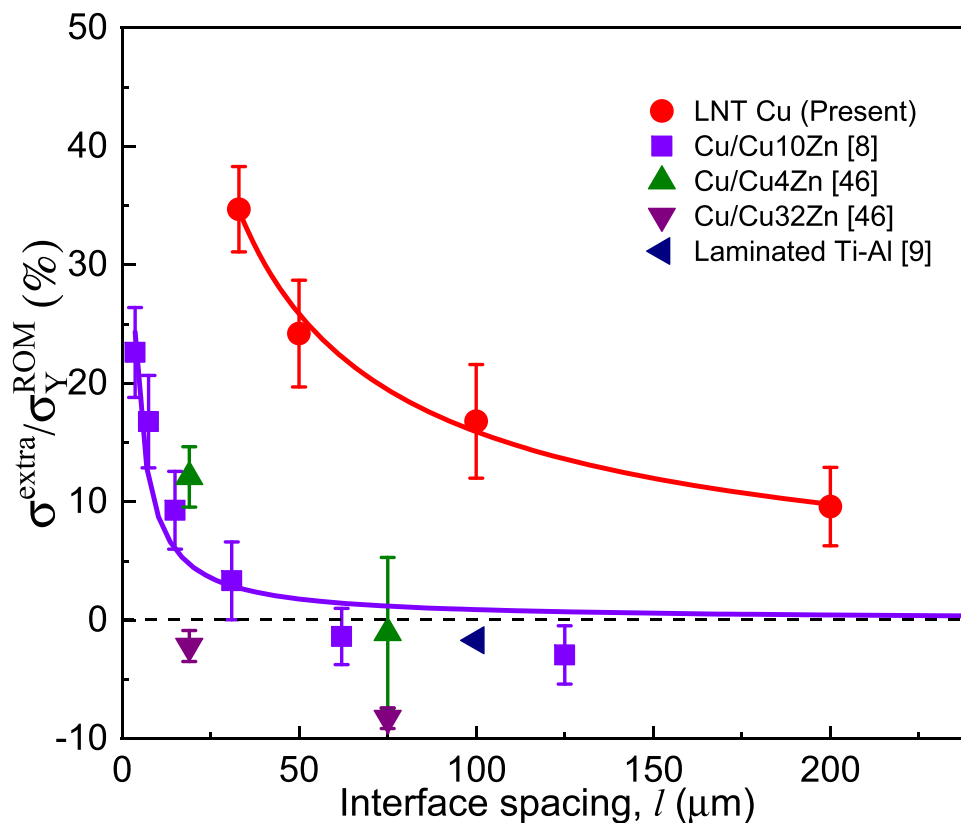


Fig. 8. The variation of normalized extra strength $\sigma_Y^{extra}/\sigma_Y^{ROM}$ with interface spacing l of LNT Cu in comparison to conventional laminated metals without nanotwins. (For interpretation of the references to color in this figure legend, the reader is referred to the web version of this article.)

interface spacing of 33 μm . Obviously, the extra strengthening effect of LNT Cu is much more significant.

Still by taking Cu/Cu10Zn [7,8] as an example, it shows that the extra strengthening stems from the interfaced-mediated deformation in conventional laminated metals. The multiple-slip dislocations dominate the plastic deformation of Cu or Cu10Zn component composed of random coarse- or nano-grains. Dislocations move to the interface and pile up by the interface as a barrier, yielding obvious strain concentration [8,16]. These piled-up dislocations at interfaces produce long-range back stresses for incoming dislocations from the same dislocation sources in the vicinity of the interface [47]. Obviously, the dislocation pile-up or strain concentration and the resultant strengthening mainly concentrate nearby the interface, forming into IAZs of $\sim 15 \mu\text{m}$ in the width [8].

On the contrary, a different deformation mechanism (Figs. 4-7) related to specific Mode II dislocations dominates the deformation of LNT Cu, due to the preferentially orientated nanotwins are parallel to TBs during tensile deformation [32,48]. Mode II dislocation nucleates from grain boundary in the columnar grain, glides parallel to TBs. That means, Mode II dislocations move in parallel to the interfaces (or TBs), which avoids dislocation piled-up or strain concentration at interfaces in LNT Cu.

The interface-mediated gradient deformation of LNT Cu originates from the progressive yielding from component ③ to ④. Component ③ with a lower yield strength yields first. Whereas component ④ with a higher yield strength deforms plastically later. As a result, the plastic tensile strain decreases across the interface from component ③ to ④. HNT structure exhibits a strong anisotropic plastic deformation where the lateral strain parallel to TBs (ϵ_y) is 7 time larger than that perpendicular to TBs (ϵ_z), i.e., ϵ_y is approximately equal to the tensile strain ϵ_x [48], the gradient distribution of ϵ_y across interfaces between two components is obvious (Fig. 4). As geometrical requirement of the strain gradient between both components, the net Burgers vector of GNDs is parallel to interfaces (or TBs), based on the classic Burgers circuit analysis [17,49]. From this, GNDs can be Mode I or/and Mode II dislocations, both of which have dislocation components parallel to TBs [32,33]. Therefore, numerous Mode I and Mode II dislocations appear near interfaces, resulting in higher total dislocation density at the interfaces than that away the interface (Fig. 7).

The GNDs induced extra strengthening can be understood in terms of isotropic and kinematic hardening [22,34]. The isotropic hardening originates from the forest dislocation hardening and corresponds to the effective stress [40]. The GNDs-associated effective stress σ_{eff} can be estimated using the developed Taylor formula by Mughrabi [50].

$$\sigma_{\text{eff}} = \alpha M \mu b \sqrt{\rho_{\text{SSD}} + \beta \rho_{\text{GND}}} \quad (5)$$

where α is a factor related to dislocation distribution, M is Taylor coefficient, μ is shear modulus, b is Burgers vector, ρ_{SSD} and ρ_{GND} are statistically stored dislocation (SSD) density and GND density, respectively. β is a factor to depicting the possibility of GNDs tangling with SSDs [50]. Since the net Burgers vectors of GNDs are parallel to those of Mode II dislocations as mentioned above and more GNDs are accumulated at the interface, rather than randomly scattered throughout the components (Figs. 6 and 7), these GNDs have less chance to tangle with Mode II dislocations and show negligible contribution to the effective stress (Fig. 3f).

Due to the superposition of stress fields from GNDs with the same sign, a directional and long-range resistance is imposed to mobile dislocations especially for Mode II dislocations with Burger vectors parallel to GNDs. The dislocation resistance is called back stress and is proportional to GND density, which can be expressed by [34,35,51]

$$\sigma_b = \kappa M \mu b d \rho_{\text{GND}} \quad (6)$$

where κ is a factor related to GND distribution [36] and d is the grain size. From the experimental observations in Figs. 4, 6 and 7, GNDs are

produced in the IAZs where gradient deformation happens, i.e., strain gradient is non-zero. Accordingly, the back stress is produced in the IAZs.

Impressively, IAZs of LNT Cu are much more dispersed, $\sim 100 \mu\text{m}$ in width, than those of other laminated materials ($\sim 15 \mu\text{m}$) [8]. The dispersed IAZ of LNT Cu is related to the formation of gradient distribution of strain gradient (or GND density) which reaches maximum at interfaces, decreases gradually away from the interface and becomes minimum in the middle of components (Figs. 4, 6 and 7). With decreasing the interface spacing, the IAZs of neighboring interfaces overlap, as shown by the constant strain gradient in Fig. 4g. That also suggests the extra strengthening extends to whole sample when the interface spacing becomes less (Figs. 5-7), rather than only concentrating in the vicinity of interfaces, thus the overall extra strengthening of LNT Cu becomes superior to other laminated structures (Fig. 8). According to Eq. (6), the back stresses induced by GNDs exhibit a similar distribution, i.e., the extra strengthening/hardening becomes stronger near the interfaces (Fig. 5). As the interface spacing decreases, the minimum value of extra strengthening becomes larger in the middle of each component, which results in an overall improvement in the extra strengthening/hardening of the LNT Cu.

Interestingly, the strain gradient at interfaces is independent on the interface spacing, which might be a salient feature of LNT structures. The strain gradient originates from deformation incompatibility due to the strength/strain discrepancy between two neighboring components beside the interface. Due to the strong anisotropic plastic deformation of nanotwinned structure, the lateral strain difference $\Delta \epsilon_y^{\text{p,A-D}}$ is equalized to the tensile plastic strain $\Delta \epsilon_x^{\text{p,A-D}}$. $\Delta \epsilon_x^{\text{p,A-D}}$ is numerically equal to the elastic strain difference $\Delta \epsilon_x^{\text{e,A-D}}$,

$$\Delta \epsilon_x^{\text{p,A-D}} = \Delta \epsilon_x^{\text{e,A-D}} = \frac{\Delta \sigma^{\text{A-D}}}{E} \quad (7)$$

where $\Delta \sigma^{\text{A-D}}$ is the flow stress difference between two components and E is elastic modulus. It follows that the strain difference can also represent the flow stress difference. As a result, the constant strain gradient and resultant extra strengthening at interfaces results in the reduction of stress discrepancy $\Delta \sigma^{\text{A-D}}$ and strain discrepancy $\Delta \epsilon_y^{\text{p,A-D}}$ between two components when the interface spacing decreases.

From experimental results, the gradient deformation mechanism across the interfaces between adjacent components allows LNT Cu to achieve superior extra strengthening over conventional laminates, which is dominated by interface-mediated strain concentration or dislocation pile-up [8,16]. The gradient deformation of LNT Cu benefits from preferentially orientated nanotwins which promote the movement of dislocations parallel to the interfaces rather than piling up at interfaces. It follows that, in addition to changing the interfacial spacing, tailoring the component microstructures by nanotwins is another effective strategy to tune the deformation mechanism of laminated metals and improve their mechanical properties.

4. Conclusion

The yield strength and work hardening at small strains of LNT Cu are higher than those predicted by ROM and increase with decreasing the interface spacing, showing superior extra strengthening than that of conventional laminated materials without nanotwins. A more dispersed IAZ, as large as 100 μm in width, is detected in LNT Cu, in which the strain gradient (or GND density) reaches maximum at interfaces and decrease gradually far away from the interface, rather than only concentrating in the vicinity of interfaces in the conventional laminated materials. The constant strain gradient at interfaces results in an improved overall extra strengthening and a reduced stress/strain discrepancy between components of LNT Cu when the interface spacing decreases. Such interface coordinated gradient deformation mechanism between neighboring nanotwinned components sheds lights on a novel

mechanism for tailoring laminated materials with superior mechanical properties.

Declaration of Competing Interest

The authors declare that they have no known competing financial interests or personal relationships that could have appeared to influence the work reported in this paper.

Acknowledgement

L. L. acknowledges financial support from the National Natural Science Foundation of China (NSFC, Grant Number. 51931010, 92163202), and the Key Research Program of Frontier Science and International partnership program (GJHZ2029), Z.C. acknowledges financial support from National Natural Science Foundation of China (NSFC, Grant Number. 52001312) and Youth Innovation Promotion Association, Chinese Academy of Sciences (CAS).

References

- [1] Y. Zhu, X. Wu, Heterostructured materials, *Prog. Mater. Sci.* (2023) 131.
- [2] H. Wu, G. Fan, An overview of tailoring strain delocalization for strength-ductility synergy, *Prog. Mater. Sci.* 113 (2020).
- [3] Y. Zhu, K. Ameyama, P.M. Anderson, L.J. Beyerlein, H. Gao, H.S. Kim, E. Lavernia, S. Mathaudhu, H. Mughrabi, R.O. Ritchie, N. Tsuji, X. Zhang, X. Wu, Heterostructured materials: superior properties from hetero-zone interaction, *Mater. Res. Lett.* 9 (1) (2020) 1–31.
- [4] A. Misra, J.P. Hirth, R.G. Hoagland, Length-scale-dependent deformation mechanisms in incoherent metallic multilayered composites, *Acta Mater.* 53 (18) (2005) 4817–4824.
- [5] L.J. Beyerlein, N.A. Mara, J. Wang, J.S. Carpenter, S.J. Zheng, W.Z. Han, R. F. Zhang, K. Kang, T. Nizolek, T.M. Pollock, Structure–property–functionality of bimetal interfaces, *JOM* 64 (10) (2012) 1192–1207.
- [6] M. Göken, H.W. Höppel, Tailoring nanostructured, graded, and particle-reinforced Al laminates by accumulative roll bonding, *Adv. Mater.* 23 (22–23) (2011) 2663–2668.
- [7] X. Ma, C. Huang, J. Moering, M. Ruppert, H.W. Höppel, M. Göken, J. Narayan, Y. Zhu, Mechanical properties of copper/bronze laminates: role of interfaces, *Acta Mater.* 116 (2016) 43–52.
- [8] C.X. Huang, Y.F. Wang, X.L. Ma, S. Yin, H.W. Höppel, M. Göken, X.L. Wu, H.J. Gao, Y.T. Zhu, Interface affected zone for optimal strength and ductility in heterogeneous laminate, *Mater. Today* 21 (7) (2018) 713–791.
- [9] M. Huang, C. Xu, G. Fan, E. Maawad, W. Gan, L. Geng, F. Lin, G. Tang, H. Wu, Y. Du, D. Li, K. Miao, T. Zhang, X. Yang, Y. Xia, G. Cao, H. Kang, T. Wang, T. Xiao, H. Xie, Role of layered structure in ductility improvement of layered Ti–Al metal composite, *Acta Mater.* 153 (2018) 235–249.
- [10] W. Chen, W. He, N. Luo, Y. Tang, Z. Chen, B. Jiang, Effect of layer thickness on the enhanced strength and ductility of laminated Ti/Al composite, *Mater. Sci. Eng. A* 859 (2022).
- [11] X. Wu, M. Yang, F. Yuan, G. Wu, Y. Wei, X. Huang, Y. Zhu, Heterogeneous lamella structure unites ultrafine-grain strength with coarse-grain ductility, *Proc. Natl. Acad. Sci. U. S. A.* 112 (47) (2015) 14501–14505.
- [12] H. Wu, G.H. Fan, M. Huang, L. Geng, X.P. Cui, H.L. Xie, Deformation behavior of brittle/ductile multilayered composites under interface constraint effect, *Int. J. Plast.* 89 (2017) 96–109.
- [13] S.H. Wu, Z.Q. Hou, J.Y. Zhang, Y.Q. Wang, K. Wu, G. Liu, J. Sun, Understanding the strength softening of Zr/Mo and Zr/Ti nanostructured multilayers, *Scr. Mater.* 172 (2019) 61–65.
- [14] H. Wang, R. Kou, H. Yi, S. Figueroa, K.S. Vecchio, Mesoscale hetero-deformation induced (HDI) stress in FeAl-based metallic-intermetallic laminate (MIL) composites, *Acta Mater.* 213 (2021).
- [15] M.-Y. Seok, J.-A. Lee, D.-H. Lee, U. Ramamurty, S. Nambu, T. Koseki, J.-i. Jang, Decoupling the contributions of constituent layers to the strength and ductility of a multi-layered steel, *Acta Mater.* 121 (2016) 164–172.
- [16] H. Zhou, C.X. Huang, X.C. Sha, L.R. Xiao, X.L. Ma, H.W. Höppel, M. Göken, X. L. Wu, K. Ameyama, X.D. Han, Y.T. Zhu, In-situ observation of dislocation dynamics near heterostructured interfaces, *Mater. Res. Lett.* 7 (9) (2019) 376–382.
- [17] M.F. Ashby, The deformation of plastically non-homogeneous materials, *Philos. Mag.* 21 (170) (1970) 399–424.
- [18] N.A. Fleck, G.M. Muller, M.F. Ashby, J.W. Hutchinson, Strain gradient plasticity: theory and experiment, *Acta Metall. Mater.* 42 (2) (1994) 475–7487.
- [19] H. Gao, Y. Huang, W.D. Nix, J.W. Hutchinson, Mechanism based strain gradient plasticity-I. Theory, *J. Mech. Phys. Solids* 47 (6) (1999) 1239–1263.
- [20] Z. Zeng, X. Li, D. Xu, L. Lu, H. Gao, T. Zhu, Gradient plasticity in gradient nano-grained metals, *Extreme Mech. Lett.* 8 (2016) 213–219.
- [21] Y. Zhang, Z. Cheng, L. Lu, T. Zhu, Strain gradient plasticity in gradient structured metals, *J. Mech. Phys. Solids* 140 (2020).
- [22] N.A. Fleck, M.F. Ashby, J.W. Hutchinson, The role of geometrically necessary dislocations in giving material strengthening, *Scr. Mater.* 48 (2) (2003) 179–183.
- [23] L.P. Kubin, A. Mortensen, Geometrically necessary dislocations and strain-gradient plasticity: a few critical issues, *Scr. Mater.* 48 (2002) 119–125.
- [24] H. Mughrabi, Deformation-induced long-range internal stresses and lattice plane misorientations and the role of geometrically necessary dislocations, *Philos. Mag.* 86 (25–26) (2006) 4037–4054.
- [25] X. Wu, P. Jiang, L. Chen, F. Yuan, Y.T. Zhu, Extraordinary strain hardening by gradient structure, *Proc. Natl. Acad. Sci. U. S. A.* 111 (20) (2014) 7197–7201.
- [26] Z. Cheng, H.F. Zhou, Q.H. Lu, H.J. Gao, L. Lu, Extra strengthening and work hardening in gradient nanotwinned metals, *Science* 362 (6414) (2018), 559–.
- [27] L. Zhu, S. Shi, K. Lu, J. Lu, A statistical model for predicting the mechanical properties of nanostructured metals with bimodal grain size distribution, *Acta Mater.* 60 (16) (2012) 5762–5772.
- [28] J. Bach, M. Stoiber, L. Schindler, H.W. Höppel, M. Göken, Deformation mechanisms and strain rate sensitivity of bimodal and ultrafine-grained copper, *Acta Mater.* 186 (2020) 363–373.
- [29] S.K. Park, K. Ameyama, J. Yoo, H. Hwang, H.S. Kim, Additional hardening in harmonic structured materials by strain partitioning and back stress, *Mater. Res. Lett.* 6 (5) (2018) 261–267.
- [30] S.K. Vajpai, M. Ota, Z. Zhang, K. Ameyama, Three-dimensionally gradient harmonic structure design: an integrated approach for high performance structural materials, *Mater. Res. Lett.* 4 (4) (2016) 191–197.
- [31] T. Wan, Z. Cheng, L. Bu, L. Lu, Work hardening discrepancy designing to strengthening gradient nanotwinned Cu, *Scr. Mater.* 201 (2021).
- [32] Z. You, X. Li, L. Gui, Q. Lu, T. Zhu, H. Gao, L. Lu, Plastic anisotropy and associated deformation mechanisms in nanotwinned metals, *Acta Mater.* 61 (1) (2013) 217–227.
- [33] Q. Lu, Z. You, X. Huang, N. Hansen, L. Lu, Dependence of dislocation structure on orientation and slip systems in highly oriented nanotwinned Cu, *Acta Mater.* 127 (2017) 85–97.
- [34] Z. Cheng, L. Bu, Y. Zhang, H. Wu, T. Zhu, H. Gao, L. Lu, Unraveling the origin of extra strengthening in gradient nanotwinned metals, *Proc. Natl. Acad. Sci. U. S. A.* 119 (3) (2022).
- [35] Z. Cheng, L. Bu, Y. Zhang, H. Wu, T. Zhu, L. Lu, Characterization of gradient plastic deformation in gradient nanotwinned Cu, *Acta Mater.* 246 (2023).
- [36] Z. Cheng, T. Wan, L. Bu, L. Lu, Effect of volume fractions of gradient transition layer on mechanical behaviors of nanotwinned Cu, *Acta Mater.* 242 (2023).
- [37] Z. Cheng, L. Lu, The effect of gradient order on mechanical behaviors of gradient nanotwinned Cu, *Scr. Mater.* 164 (2019) 130–134.
- [38] W.D. Nix, H. Gao, Indentation size effects in crystalline materials: a law for strain gradient plasticity, *J. Mech. Phys. Solids* 46 (3) (1998) 411.
- [39] J.I. Dickson, J. Boutin, L. Handfield, A comparison of two simple methods for measuring cyclic internal and effective stresses, *Mater. Sci. Eng. A* 64 (1984) L7–L11.
- [40] X. Feaugas, On the origin of the tensile flow stress in the stainless steel AISI 316 L at 300 K: back stress and effective stress, *Acta Mater.* 47 (13) (1999) 3617–3632.
- [41] U.F. Kocks, H. Mecking, Physics and phenomenology of strain hardening: the FCC case, *Prog. Mater. Sci.* 48 (3) (2003) 171–273.
- [42] S. Allain, O. Bouaziz, A quantitative modeling of the unloading behavior of metals during a tensile test, *Int. J. Mat. Res.* 101 (12) (2010) 1497–1502.
- [43] L. Bu, Z. Cheng, Y. Zhang, H. Wu, T. Zhu, L. Lu, Trans-twin dislocations in nanotwinned metals, *Scr. Mater.* (2023) 229.
- [44] J. Wang, Q. Zhou, S. Shao, A. Misra, Strength and plasticity of nanolaminated materials, *Mater. Res. Lett.* 5 (1) (2016) 1–19.
- [45] Y. Zhang, J.G. Gigax, T.J. Nizolek, J.S. Carpenter, M.M. Schneider, N. Li, L. Capolungo, R.J. McCabe, Tensile and failure behaviors of Cu/Nb nanolaminates: the effects of loading direction, layer thickness, and annealing, *Acta Mater.* 240 (2022).
- [46] Z. Cao, Z. Cheng, W. Xu, L. Lu, Effect of work hardening discrepancy on strengthening of laminated Cu/CuZn alloys, *J. Mater. Sci. Technol.* 103 (2022) 67–72.
- [47] Y. Zhu, X. Wu, Perspective on hetero-deformation induced (HDI) hardening and back stress, *Mater. Res. Lett.* 7 (10) (2019) 393–398.
- [48] Z.S. You, L. Lu, K. Lu, Tensile behavior of columnar grained Cu with preferentially oriented nanoscale twins, *Acta Mater.* 59 (18) (2011) 6927–6937.
- [49] G.A. Malygin, Dislocation mechanism of dynamic polygonization of a crystal caused by its bending, *Phys. Solid State* 44 (2002) 1249–1253.
- [50] H. Mughrabi, The α -factor in the Taylor flow-stress law in monotonic, cyclic and quasi-stationary deformations: dependence on slip mode, dislocation arrangement and density, *Curr. Opin. Solid St. M.* 20 (6) (2016) 411–420.
- [51] Y. Zhang, K. Ding, Y. Gu, W. Chen, Y.M. Wang, J. El-Awady, D.L. McDowell, T. Zhu, Modeling of microscale internal stresses in additively manufactured stainless steel, *Modell. Simul. Mater. Sci. Eng.* 30 (7) (2022).